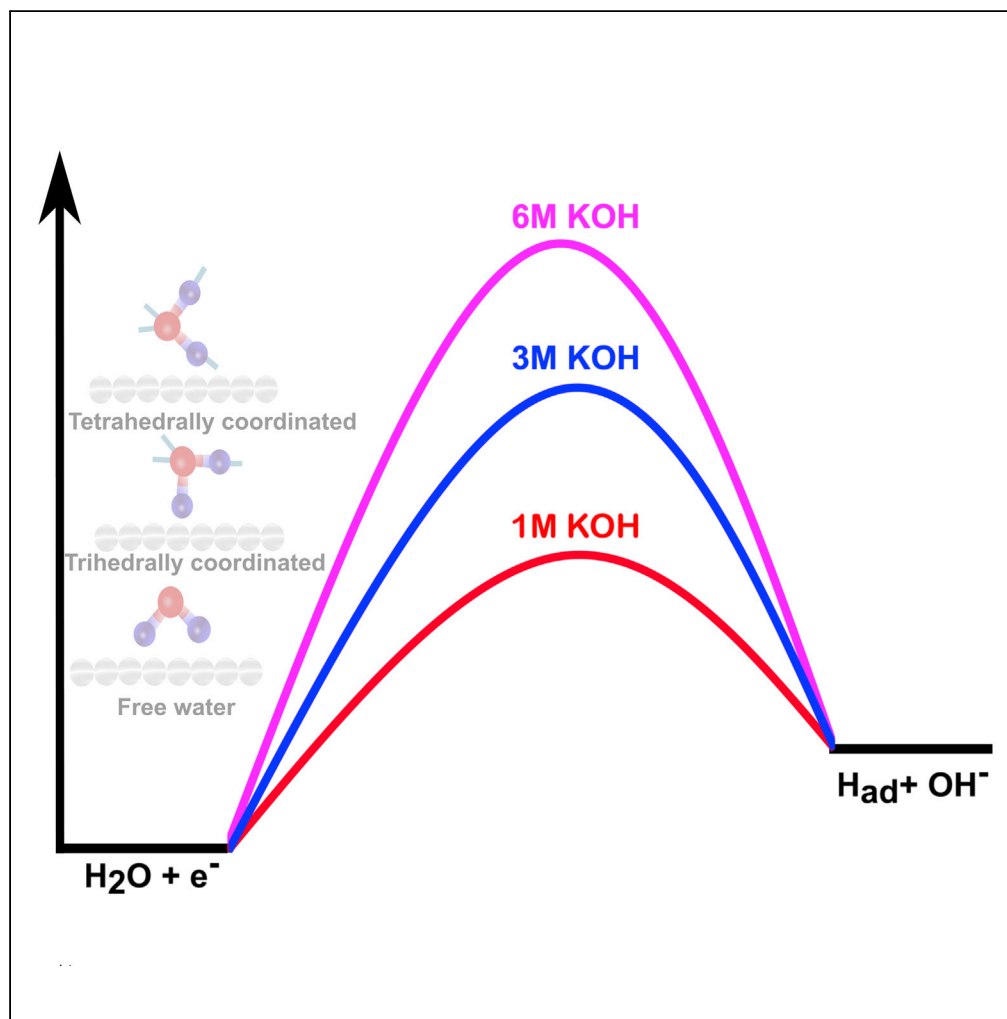## Article
Role of water structure in alkaline water electrolysis

Anku Guha, Mihir Sahoo, Khorsed Alam, D. Krishna Rao, Prasenjit Sen, Tharangattu N. Narayanan

aguha2012@gmail.com (A.G.)
prasen@hri.res.in (P.S.)
tnn@tifrh.res.in (T.N.N.)

Highlights
A mechanistic insight into the alkaline hydrogen evolution reaction (HER) is provided

The role of water structure/coordination variation in HER kinetics is studied

The interfacial water structure variation is studied using *in situ* Raman studies

The Pt–H coverage changes during the HER process are also investigated

Article

Role of water structure in alkaline water electrolysis

Anku Guha,[1,*] Mihir Sahoo,[2] Khorsed Alam,[2] D. Krishna Rao,[1] Prasenjit Sen,[2,*] and Tharangattu N. Narayanan[1,3,*]

SUMMARY

Herein, with the help of experimental and first-principles density functional theory (DFT)-based studies, we have shown that structural changes in the water coordination in electrolytes having high alkalinity can be a possible reason for the reduced catalytic activity of platinum (Pt) in high pH. Studies with *polycrystalline* Pt electrodes indicate that electrocatalytic HER activity reduces in terms of high overpotential required, high Tafel slope, and high charge transfer resistances in concentrated aqueous alkaline electrolytes (say 6 M KOH) in comparison to that in low alkaline electrolytes (say 0.1 M KOH), irrespective of the counter cations (Na$^+$, K$^+$, or Rb$^+$) present. The changes in the water structure of bulk electrolytes as well as that in electrode-electrolyte interface are studied. The results are compared with DFT-based analysis, and the study can pave new directions in studying the HER process in terms of the water structure near the electrode-electrolyte interface.

INTRODUCTION

Hydrogen evolution reaction (HER) and oxygen evolution reaction (OER) are the two key reactions in a water electrolyzer. Understanding the mechanisms of HER and OER is necessary to improve the energy efficiency of green hydrogen production via water splitting. The differences in the catalytic activities of different metals toward HER in an acidic medium (0.5M H_2SO_4) is assumed to be explainable via the Sabatier principle (Laursen et al., 2012). According to the Sabatier principle, HER activity depends on metal-hydrogen (ΔE_{M-H}) binding strength, which leads to a volcano type plot when using ΔE_{M-H} as a descriptor of the activity of metals for HER (Nørskov et al., 2005). In this scenario, metals such as Pt or Pt-group metals are excellent electrocatalysts for HER due to their thermoneutrality for hydrogen adsorption (optimum metal-hydrogen binding energy leads to $\Delta E_{M-H} \sim 0$ eV) (Morales-Guio et al., 2014). But this reasoning cannot be extended to the alkaline HER, in particular, it fails to explain the sluggish reaction kinetics of HER on Pt in alkaline media. One can observe presence of underpotential (H_{UPD}) and overpotential deposited (H_{OPD}) hydrogen in alkaline medium by applying potential-controlled surface-enhanced spectroscopy on surfaces of Pt (Mahmood et al., 2018; Zhu et al., 2020). Due to the limited availability of protons in low acidic conditions, water is a more likely source of adsorbed hydrogen, and the dissociation energy of water adds an extra contribution to the Gibbs free energy of the Volmer step ($H_2O + e^- \rightarrow *H + OH^-$). Hence, the rate determining steps of HER are different in alkaline and acidic electrolytes, and a clear understanding of the mechanism is essential for designing next-generation cost-effective catalysts for this process.

In the past, several hypotheses have been put forward to explain the pH dependency of HER kinetics on Pt surfaces (Cheng et al., 2018; Danilovic et al., 2012; Huang et al., 2021; McCrum and Janik, 2016; Sheng et al., 2015; Zheng et al., 2018; Zhu et al., 2020). It was initially suggested that the stronger Pt–H binding energy in alkaline media, which can be correlated with shifts in the H_{UPD} peaks with pH, (Sheng et al., 2015) is the sole reason for the slower rate of HER in alkaline electrolytes. However, it was later shown that the ΔE_{M-H} is an inherent property of a metal, and the variations in H_{UPD} peak positions are due to the competitive mechanism between *H and water adsorption, where the latter becomes weaker at high alkalinity (Cheng et al., 2018; Sheng et al., 2015; Zheng et al., 2018). Alternatively, "specific adsorption of cations and their different capability in stabilizing/destabilizing *OH" has also been proposed as the origin of shift in the H_{UPD} peaks (Liu et al., 2019).

In a different work, the binding energy of Pt–H_2O instead of Pt–H binding energy was considered to explain the pH-dependent HER kinetics of Pt in a highly alkaline medium. According to this hypothesis,

the Pt−H$_2$O binding energy decreases with increasing pH of the electrolytes, whereas the apparent Pt−H binding energy increases, leading to the slower kinetics of HER on Pt in alkaline media (Sheng et al., 2015; Zhu et al., 2020). According to Markovic et al., the slower kinetics of HER on Pt in alkaline media is due to the high energy barrier for the dissociation of water to generate H$_{ad}$ (Subbaraman et al., 2011). According to them, the energy barrier to dissociate water can be minimized by using Ni(OH)$_2$-coated Pt, whereas the reason behind the high activation energy for water dissociation in alkaline medium was not known. According to a different hypothesis, because the potential of zero free charge (pzfc) of Pt is pH independent, the HER of Pt shifts further away from the pzfc of Pt with increasing pH, which makes water more rigid (Gonella et al., 2021; Ledezma-Yanez et al., 2017; Ojha et al., 2022; Sarabia et al., 2019). Lin-fan Shen et al. have shown that the pH-dependent kinetics on Pt surfaces and the Ni-induced high activity are driven by the structure of the interfacial water (Shen et al., 2020). It was shown by *in situ* Raman studies that, although the water structure does not get affected by the applied potential in an acidic medium, the population of different water co-ordinations in Pt and Pt-Ni are different in an alkaline medium. It is shown that "free-water" type (dangling O−H bonds) is available in Pt-Ni-0.1 M NaOH system, whereas almost no such water coordination is available in Pt-0.1 M NaOH system at a similar potential. This has been correlated with the higher activity of Pt-Ni in alkaline medium in comparison to the sluggish activity of bare Pt electrodes.

It is known that water structure stabilization happens over the H$_{OPD}$ hydrogen layer, and hence electrolyte-induced changes in the structure of the interfacial water may be behind the differences in the HER activity with different electrolytes (Li et al., 2010). Raman and infrared (IR) studies show that H$_{OPD}$ coverage is higher in alkaline than in acidic medium, where it has been explained that H$_{OPD}$ migrates to 3f2 sites of Pt in acidic media giving half of the coverage, whereas this kind of migration is forbidden in alkaline media leading to a full coverage (Ramaker and Roth, 2015). Hence, it is apparent that the structural changes in water are important to understand the changes in HER kinetics with pH as well as the nature of the electrolyte cations.

We have recently shown that the HER activity of *polycrystalline* Pt decreases with increasing lithium ion (Li$^+$) concentration (Guha et al., 2018a, 2020; Guha and Narayanan, 2020). Our theoretical studies suggest that the apparent Pt−H binding energy decreases with increasing Li$^+$ concentration, which can alter the HER kinetics in tune with the hydrogen-binding energy hypothesis. Several other studies suggest that the HER activity of Pt decreases from Li$^+$ to Cs$^+$ in the order LiOH > NaOH > KOH > RbOH > CsOH, as Cs$^+$ weakens the Pt−H$_2$O bonds the most (Chen et al., 2017). Despite extensive studies using different techniques, the pH dependency of HER kinetics on Pt remains an unsolved problem, and here we explore electrolyte-induced structural changes in both bulk and interfacial water with the help of Raman and *in situ* Shell Isolated Nanoparticles Enhanced Raman Scattering (SHINERS) studies. Additional evidence of electrolyte-induced changes in the water structure is obtained by using *ex situ* ^{1}H NMR, *ATR-FTIR*, and density functional theory (DFT)-based first-principles studies.

The HER activity of a *polycrystalline* Pt electrode was tested in increasing concentrations of KOH, NaOH, and RbOH (between 0.1 and 6 M). Structural changes in the interfacial water were monitored by analyzing the −OH stretching bands of water and their dependence on the applied bias using SHINERS. Studies on both oxidative (OER) and reductive (HER) potentials are conducted and correlated with the room temperature HER voltammetry/impedance studies.

RESULTS AND DISCUSSIONS

The HER linear sweep voltammograms (LSVs) of Pt in KOH solutions of increasing concentrations are shown in Figure 1A. The changes in the pH of the electrolytes are measured, and the values can be seen in Table S1. The overpotential required to achieve a current density of 2 mA cm^{-2} (geometrical area) is 19 mV in 0.1 M KOH (pH: 13), 27 mV in 1 M KOH, 72 mV in 3 M KOH, and 131 mV in 6 M KOH. The nearly linear increase of the current with increasing negative overpotential in 0.1 M KOH is due to the low ionic conductivity of the electrolyte (0.0241 S cm^{-1} at 25°C (Gilliam et al., 2007)) as compared with 0.215 S cm^{-1} at 25°C in 1 M KOH (Gilliam et al., 2007).

Furthermore, to understand the effects of such electrolyte changes in Pt/C, the HER activity of Pt/C (20 wt%) is also studied with varying concentration of KOH. With increasing the KOH concentration from 0.1 M to 1 M, the HER activity of Pt/C (20 wt%) increases, whereas from 1 M to 6 M KOH, the HER activity of Pt/C (20 wt %) decreases as shown in Figure S1A. The overpotential required to achieve 0.5 mA cm^{-2} current density
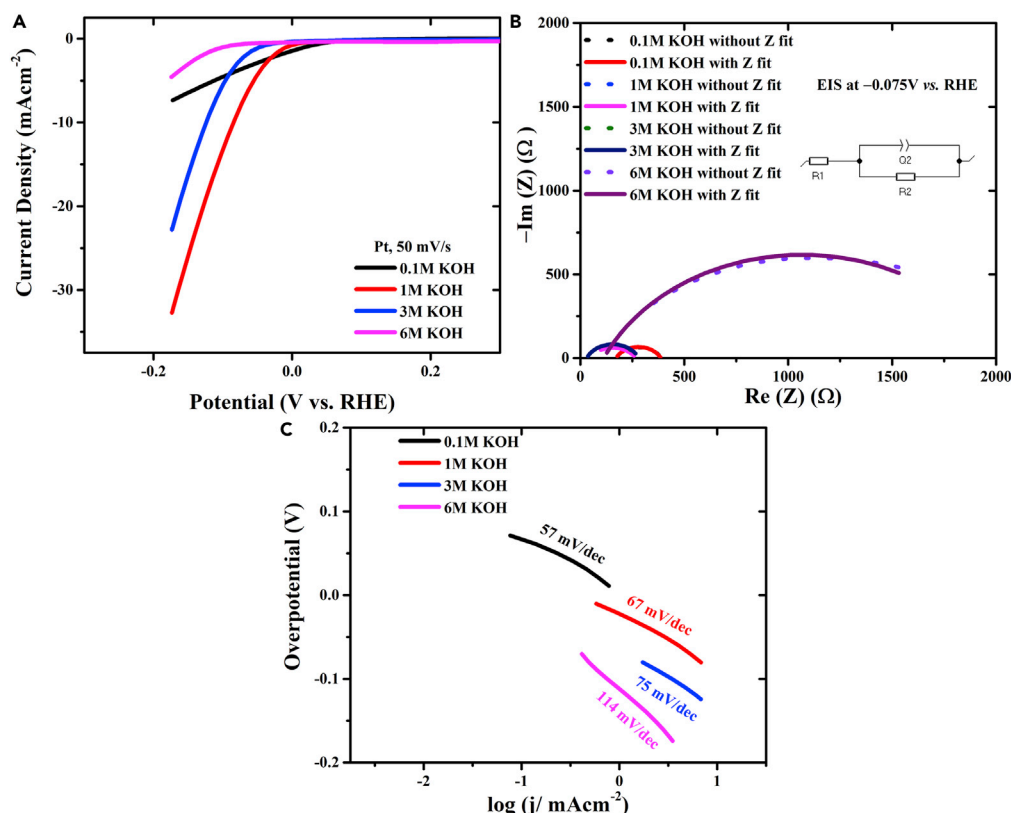
Figure 1. HER performance of *polycrystalline* Pt in different concentrations of KOH

(A) Linear sweep voltammograms at 50 mVs^{-1} of Pt in 0.1 (black), 1 (red), 3 (blue), and 6 (purple) M KOH.

(B) Nyquist plots (solid lines) at −0.075 V versus RHE obtained with a superimposed sine wave 10 mV in amplitude within the frequency range between 7 MHz and 100 mHz in the same electrolyte used in Figure 1A. The dotted lines correspond to the best fit to a Randles circuit. Inset: the Randles circuit.

(C) HER Tafel plots in 0.1 (black), 1 (red), 3 (blue), and 6 (purple) M KOH.

(electrochemically active surface area (ECSA, shown in Table S2)) for Pt/C is 36 mV in 0.1 M KOH, 17 mV in 1 M KOH, 57 mV in 3 M KOH, and 92 mV in 6 M KOH. According to Wang et al., this anomaly in the HER reactivity of Pt/C (20 wt%) from 0.1 M to 1 M is due to massive formation of H_3O^+ on the catalytic surface during the course of electrolysis (Wang et al., 2019). Our LSV results also show similar differences in the HER LSVs of Pt and Pt/C while changing the concentration from 0.1 M to 1 M KOH. The overpotentials to achieve 2 mA cm^{-2} current density at a *polycrystalline* Pt in 0.1 M NaOH and RbOH electrolytes are found to be ~16 and ~24 mV, respectively, where the values increased to ~97 and ~141 mV, respectively for 6 M NaOH and 6 M RbOH (Figure S2, Table S3). According to Xue et al. the HER activity of *polycrystalline* Pt decreases with increasing hydration energy of the alkali metals present in the electrolyte ($Li^+ < Na^+ < K^+ < Cs^+$) (Xue et al., 2018). Here also the HER activity of *polycrystalline* Pt decreases from $Na^+ > K^+ > Rb^+$ both in 0.1 and 6 M concentration (Table S3). The HER performance of *polycrystalline* Pt decreases with increasing NaOH or RbOH concentration. Hence, the LSV analyses show that the HER activities of Pt, irrespective the nature of Pt surface, decrease with high concentration of NaOH/KOH/RbOH.

Electrochemical impedance spectra (EIS) were recorded at −0.075 V versus RHE using a sine wave with an amplitude of 10 mV in the frequency range of 7 Mz to 100 mHz. Nyquist plots in 0.1, 1, 3, and 6 M media and the corresponding fits to a Randles circuit are shown in Figure 1B. The charge transfer resistance and capacitance (constant phase element (CPE)) values obtained from the best fit are summarized in Table S4. The solution resistance (R1) is ~156 Ω in 0.1 M KOH and decreases to 30 Ω in 3 M KOH but increases again to 112 Ω for 6 M KOH due to ion pairing (Guha et al., 2020). The charge transfer resistance (R2) increases from 215 Ω in 0.1 M KOH to 1935 Ω in 6 M KOH, indicating the decrease in the HER activity with increasing KOH concentration. The big dispersion in the capacitance may be due to high
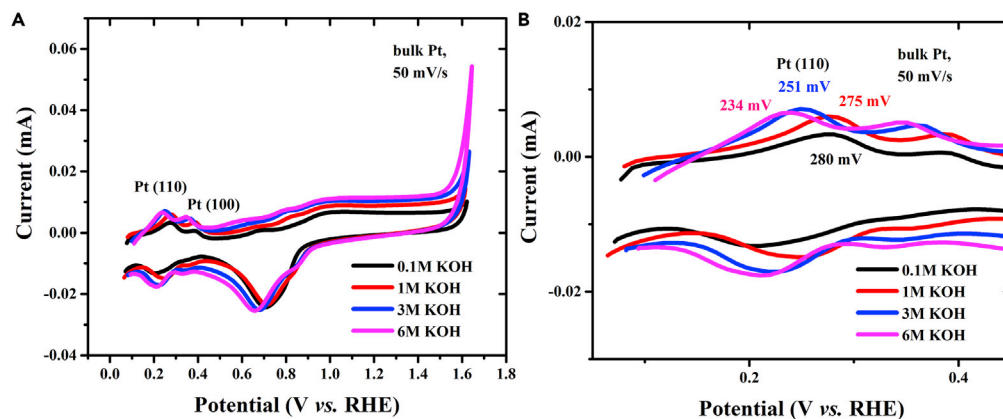
Figure 2. CVs of *polycrystalline* Pt in different concentrations of KOH
The CVs, (A) in the entire voltage scan window and (B) the H_{UPD} zoomed area, of Pt in varying KOH concentrations. The shifts in H_{UPD} peaks indicating the changes in the apparent Pt−H binding energies with different KOH concentrations.

concentration of supporting ions or the *polycrystalline* nature of the Pt electrode (Guha and Narayanan, 2020).

The Tafel slopes are calculated at 5 mV/s scan rate at the HER onset potential region in argon-saturated electrolytes. A Tafel slope of ~57 mV/decade (mV/dec) was obtained for HER in 0.1 M KOH, in good agreement with previous reports (Guha and Narayanan, 2020; Yu et al., 2018). The Tafel slope increases with increasing KOH concentration up to a value of ~114 mV/dec in 6 M KOH. The increment in the Tafel slope indicates a change in the HER kinetics, and it can be attributed to the changes in the rate determining step. It can be assumed that the rate determining step of the HER on Pt changes from the transfer of a proton-coupled electron to an adsorbed hydrogen (Heyrovsky step in 0.1 M KOH) to the adsorption of hydrogen (Volmer step in 6 M KOH), which is attributed to the changes in water dissociation energy, as discussed later (Faid et al., 2020).

According to the hydrogen binding energy (HBE) hypothesis, the apparent $\Delta E_{M\text{-}H}$ can be calculated from analyzing the cyclic voltammogram (CV) of Pt using the relation $\Delta E_{M-H} = -FE_{peak}$, where *F* is the Faraday constant and E_{peak} is the potential of H_{UPD} peaks on Pt (100) or (110) (Sheng et al., 2015). Figure 2 confirms that the position of the (110)-H_{UPD} desorption peak shifts from 280 mV versus RHE in 0.1 M KOH to 234 mV versus RHE in 6 M KOH. The same trend is obtained with Pt/C (20 wt%) too, as shown in Figure S1B, i.e. the apparent hydrogen adsorption energy decreases with increasing KOH concentration, making hydrogen adsorption the rate determining step. To further verify this hypothesis, KOH was replaced with NaOH and RbOH (Figure S3). In both NaOH and RbOH, $\Delta E_{Pt\text{-}H}$ also decreases with increasing concentration from 0.1 M to 6 M.

It has to be noted that in contrast to a high acidic medium, water plays an important role to generate *H in low acidic, neutral, and alkaline media. It has been identified that water can mainly have three different co-ordinations environments (namely tetrahedrally coordinated, trihedrally coordinated, and free water) in an electrolyte depending on the degree of hydrogen bonding within the solution. As the degree of hydrogen bonding of water increases, the activation energy required for its dissociation increases in the order: free water < trihedrally coordinated water < tetrahedrally coordinated water (Shen et al., 2020). It is important to point out that this was only an assumption in Shen et al. (2020). We explore this in more detail in our DFT based calculations. Experimental observations of the changes in the relative population of water molecules in each of these coordination environments at different alkali concentration are discussed below.

The *ex situ* Raman spectra of different electrolytes are shown in Figure S4. The details of the *ex situ* Raman set up and Raman scattering collection details are given in the experimental section and supporting information. Clear changes with varying alkali metal cations concentration can be observed in the −OH stretching region of H_2O (between 3000 and 3700 cm^{-1}). This broad peak corresponding to −OH stretching mode can be deconvoluted into three Gaussians peaks, assigned to tetrahedrally coordinated water (solid or ice-like water, ~ 3200 cm^{-1}), trihedrally coordinated water (liquid like water, ~ 3400 cm^{-1}), and free water
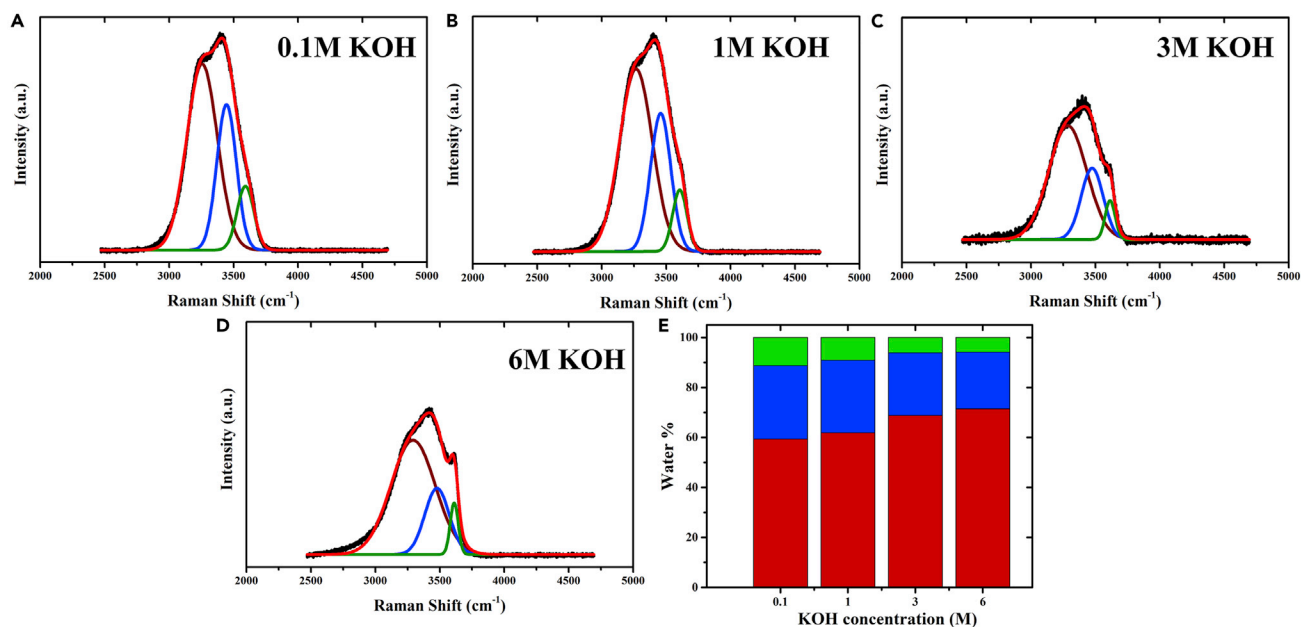
Figure 3. *Ex situ* Raman spectrum

Raman scattering spectra in the −OH stretching region of (A) 0.1 M KOH, (B) 1 M KOH, (C) 3 M KOH, and (D) 6 M KOH. (E) Relative population of the different types of water in each of these solutions: tetrahedral (red), trihedral (blue), and hydrogen-bond free (green) water.

($\sim$3600 cm^{-1}), respectively (Stefanski et al., 2018). The contributions of each of these kinds of water to the overall spectrum at different KOH concentration are shown in panels (A)–(D) of Figure 3. Similar changes can be seen in NaOH and RbOH electrolytes (Figures S5 and S6).

The relative population of each of the three water environments with increasing KOH concentration is shown in Figure 3E. The percentage (%) of the population of tetrahedrally coordinated water increases from $\sim$58% in 0.1 M KOH to $\sim$69% in 6 M KOH, whereas the population of trihedrally coordinated water and free water decreases gradually from $\sim$31% to $\sim$24% (trihedral) and from $\sim$11% to 6% (free), respectively (which are tabulated in the Table S5). Similar trends are observed in NaOH and RbOH electrolytes too.

Du et al. have recently provided evidence based on computational calculations that alkali metal cations can affect the water-water coordination (Du et al., 2007). They observed that the hydration number decreases and the water-water coordination number increases with increasing concentration of alkali metal cations. This is in line with our observation that as the concentration of KOH/NaOH/RbOH increases, the % of tetrahedral water increases. Similarly, Botti et al. have shown that by increasing NaOH concentration, the first neighboring water layer remains unaltered but the second neighboring layer contracts, which confirms that the water H-bonding network extends as the NaOH concentration increases (Botti et al., 2004). In these electrolytes, KOH/NaOH/RbOH dissociates to K$^+$/Na$^+$/Rb$^+$ and OH$^-$ ions, where they act as monovalent charge centers generating an electric field. These electric fields polarize the water molecules, resulting in more H-bonding between them. Hence, more tetrahedrally coordinated water molecules are formed with increasing KOH/NaOH/RbOH concentrations (Wang et al., 2020).

^{1}H NMR spectroscopy of these aqueous electrolytes containing varying KOH concentrations is conducted using a coaxial NMR tube having D$_2$O as a locking agent. The spectra are shown in Figure 4. The chemical shift of the proton of DI water is found to be at $\sim$ 4.7 ppm. Grimaud et al. have shown that increasing the concentration of LiTFSI (lithium bis(trifluoromethanesulfonyl)imide) salt in water from 0 to 20 m changes the chemical shift of protons up-field from 4.7 ppm (0 m LiTFSI) to 3.4 ppm (20 m LiTFSI) (Dubouis et al., 2018). This has been attributed to the increase in the percentage of hydrogen-bond free water content (Dubouis et al., 2018). On the contrary, in the present study, the increase in KOH concentration from 0 M to 6 M results in a progressive down-field chemical shift of the NMR signal of H$_2$O from 4.7 ppm (pure water) to 4.8 ppm (6 M KOH), as shown in Figure 4A. According to Oka et al., the downfield shift of water proton peak can be
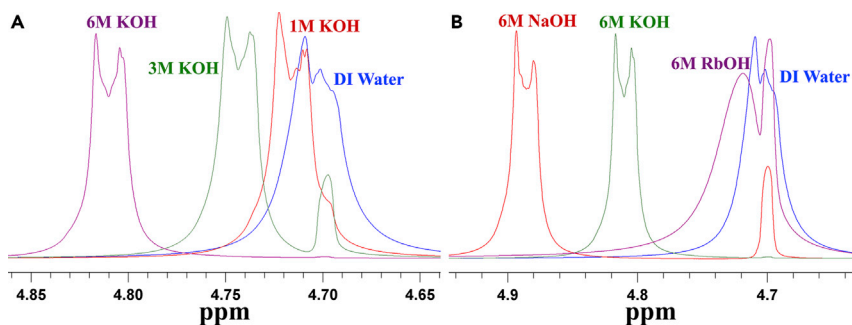
Figure 4. NMR spectrum of electrolytes
^{1}H NMR spectra of (A) DI water and electrolyte having different KOH concentrations and DI water and (B) 6 M NaOH, 6 M KOH, and 6 M RbOH.

due to strong hydrophilic interactions in water clusters (Oka et al., 2019). To further verify this observed ^{1}H NMR shift, we have performed ^{1}H NMR using 10 mM sodium trimethylsilylpropanesulfonate (DSS) as an internal standard in 90% D_2O + 10% water in the internal tube and pure water or 6 M KOH in the outer tube. The results are shown in Figure S7 and confirm that the water peak shifts downfield by 0.1 ppm in 6 M KOH. To exclude a possible effect of impurities due to corrosion of the glass surface of the NMR tube by the strongly alkaline 6 M KOH solution, inductively coupled plasma-atomic emission spectroscopy (ICP-AES) measurements of DI water and 6 M KOH are performed after keeping the solution in the glass tube first for 1 h and then for 2 days, and the results are shown in Figures S8 and S9. It is clear that even after 48 h, negligible amount of silicon or boron is present (<10 ppm) in the 6 M KOH solution, discounting any effects of such ions in the observed NMR peak shift. Similar effects are observed with other electrolytes such as NaOH and RbOH (Figure 4B). Better shielding effect and lesser Lewis's acidity of Rb^+ are responsible for a lower shift of ^{1}H NMR peak in 6 M RbOH. Furthermore, it is also verified that similar or large silicon contamination in water cannot result in the observed changes in the ^{1}H NMR by control experiments with purposeful addition of silicon salt (0.5 vol % sodium silicate, data not shown).

Fourier transform infrared spectroscopy–attenuated total reflectance (*ATR-FTIR*) spectroscopy was performed (details are in STAR Methods) in electrolytes with increasing NaOH/KOH/RbOH concentration (Figure S10). With increasing the concentration, the H-OH bending frequency is found to be blue-shifted from ~1634 cm^{-1} (for DI water) to ~1641 cm^{-1} (for 6 M NaOH and 6 M KOH) and ~1638 cm^{-1} (for 6 M RbOH), indicating that with increasing NaOH or KOH or RbOH, the H-bonding network increases, as H−OH bending mode is a powerful indicator of the strength of H-bonding (Figures S10A, S10C and S10E) (Seki et al., 2020). Increasing the concentration of KOH results in a broadening of the −OH stretching region below 3000 cm^{-1}, an effect also observed in NaOH and RbOH solutions (Figures S10B, S10D, S10F), suggesting that the concentration of tetrahedrally coordinated water increases with increasing concentration of KOH, NaOH, or RbOH. Further to check the population of different types (co-ordinations) of water molecules, the −OH stretching regions of *ATR-FTIR* spectra are deconvoluted with four Gaussian peaks (Figure S11) (Barbara and Aroulmoji, 2020), namely, quasi-crystalline water ($[(H_2O)_nOH]^-$) (~3000 cm^{-1}), solid-like water or tetrahedrally coordinated water (~3200 cm^{-1}), liquid-like water or trihedrally coordinated water (~3400 cm^{-1}), and free water (~3600 cm^{-1}). The population of four different types of water is shown in Table S6 in supporting info. It is clear from Table S6 that in 6 M NaOH, KOH, or RbOH, the populations of quasi-crystalline water and tetrahedrally coordinated water are higher than in pure DI water, which is consistent with our *ex situ* Raman as well as ^{1}H NMR observations.

The interfacial water and its structure play a significant role in HER kinetics. To check the structural changes of interfacial water with changing potential as well as changing the concentration of KOH, we have employed an *in situ* shell-isolated nanoparticle-enhanced Raman spectroscopy (SHINERS) using thin SiO_2-coated Au nanoparticles (Figure S12) drop casted over the Pt electrode. Unlike in *ex situ* Raman study, with *in situ* SHINERS, the HOH bending mode at ~ 1600 cm^{-1} can be seen due to the plasmon-enhanced Raman scattering effect (Figures 5A–5E) (Huang et al., 2021). The vibration mode at ~ 1330 cm^{-1} is commonly observed in metals deposited on SiO_2 corresponding to the Si−O stretching mode (Ataka and Osawa, 1998). With increasing concentration of KOH, the bending mode of water becomes more prominent, which indicates that with increasing KOH concentration the water becomes more ordered (Li
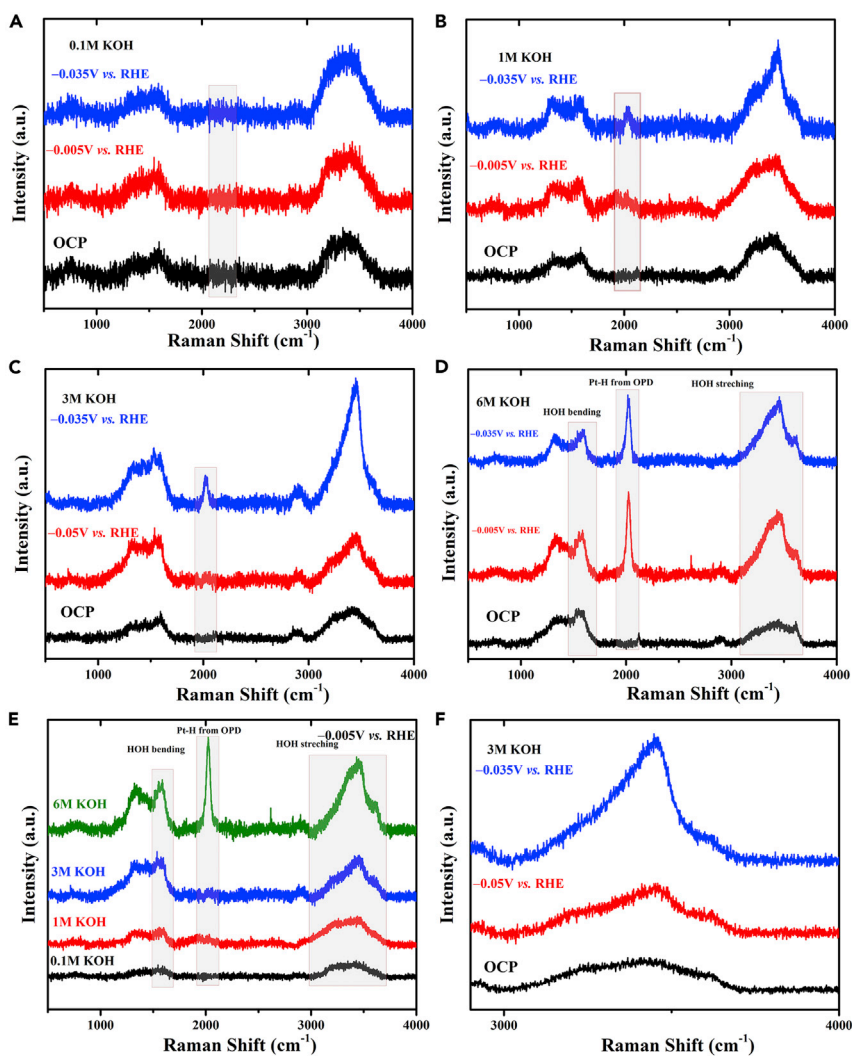
Figure 5. *In situ* surface enhanced Raman spectrum in reductive potentials
In situ SHINERS spectra of (A) 0.1 M KOH, (B) 1 M KOH, (C) 3 M KOH, and (D) 6 M KOH. (E) Comparison of 0.1, 1, 3, and 6 M KOH at −0.005 V versus RHE. (F) Shows the water stretching (zoomed in) mode of 3 M KOH, indicating the change in the structure with the potential.

et al., 2019) (we have found similar observation in NaOH, Figure S13). The bending mode of water remains almost unaltered (frequency of the bending mode of water) when the concentration of KOH or the applied electrode potential is varied (Figures 5A–5D). At sufficiently negative potentials, a peak, which is more intense in more concentrated solutions, appears around ∼2028–2021 cm^{-1} (Figures 5B, 5C, 5D and 5E), corresponding to the Pt−H stretching of the H adsorbed on top of Pt, usually known as H$_{OPD}$ (Ogasawara and Ito, 1994; Ren et al., 1999). The Pt−H stretch appears at a considerably lower frequency than that observed by Nichols and Bewick (Bewick and Russell, 1982) and Kunimatsu et al. (∼2090 cm^{-1}) due to the negative shift of the potential window of water with increasingly alkaline pH (Kunimatsu et al., 2005, 2006, 2007). This is intense in alkaline medium, as one expects a full coverage of hydrogen over Pt unlike in case of acidic medium, as discussed before and seen by others (Zhu et al., 2020). The Pt−H bond is very sensitive toward the applied potential. With increasing the potential from −0.005V to −0.035V in 6 M KOH, the Pt−H bond red shifted from ∼2023 cm^{-1} to ∼2021 cm^{-1}. Higher H$_{OPD}$ coverage over Pt with increasing KOH concentrations can be due to the Pt−H−H$_2$O complex formation, as predicted by others (Zhu and Shao, 2022). This higher H$_{OPD}$ coverage can decrease the number of active sites on Pt, eventually decreasing the rate of the H-adsorption (Volmer step). This makes the Volmer step the rate determining step in the HER process at higher alkali concentrations, also seen from the fact that the Tafel
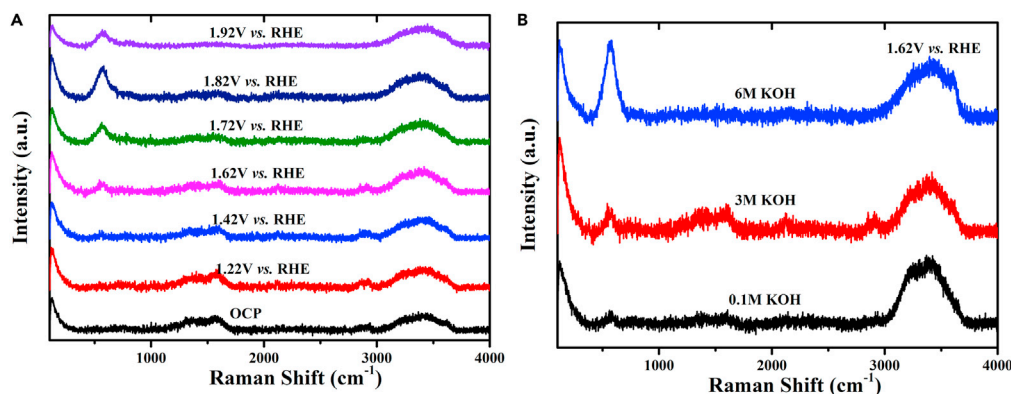
Figure 6. *In situ* **surface enhanced Raman spectrum in oxidative potentials**
In situ SHINERS spectra of Pt (A) in 3M KOH with varying the potential and (B) at 1.62V versus RHE varying the KOH concentration.

slope is higher at higher alkali concentrations. On the other hand, the higher H_{OPD} coverage can also increase the distance between Pt surface and water, retarding the electron transfer for the reduction of H_2O (Zhu and Shao, 2022). From Figure 5, it is observed that with increasing the potential from OCP (shown in Table S7) to −0.035V, the tetrahedrally coordinated water gradually converted to trihedrally coordinated water in 1 M, 3 M (zoomed in Figure 5F), and 6 M KOH. This is concluded from the observation that the intensity of the Raman peak at ∼ 3400 cm^{-1} increases, whereas that at ∼ 3200 cm^{-1} decreases with increasing alkali concentration but has minimum effect in 0.1 M KOH.

Similar *in situ* SHINERS spectra are also observed for different concentrations of NaOH and RbOH too, as shown in Figure S13 and S14, respectively. According to Shinagawa et al., the increment in the Tafel slope in Figure 1C can happen not only due to the change in the rate determining step but also due to the increase in the hydrogen coverage of the catalyst during the course of the electrolysis (Shinagawa et al., 2015). It is apparent from the *in situ* SHINERS experiments that with increasing concentration of KOH/NaOH, the H_{OPD} peak of Pt increases.

We further extended the *in situ* SHINERS experiment to the oxidative potential range, i.e. high anodic potential range, from OCP (shown in Table S7) to 1.92 V versus RHE in 3 M KOH, and the data are shown in Figure 6A. A broad peak around 570 cm^{-1} appears due to PtO_x formation (Huang et al., 2016). With increasing the potential from OCP to 1.92 V versus RHE, the PtO_x formation (intensity) over Pt increases, as seen in Figure 6A. The H–OH bending peak at 1600 cm^{-1} is slightly affected with applied potential as well as with concentration, whereas the −OH stretching peak at 3000 cm^{-1} to 3600 cm^{-1} remains unaltered. The mechanism of OER alone needs further investigation and will be reported later. Nevertheless, it is evident from Figure 6B that the PtO_x intensity increases as the concentration increases, whereas the concentration or potential did not affect the −OH stretching mode much in the OER process.

To elucidate the experimental observations and to check if the assumed order of water dissociation energy for water molecules in the three different coordination environments is correct, we have calculated this quantity using first-principles DFT. To the best of our knowledge, dependence of water dissociation energy on coordination of water molecules has not been calculated from first principles yet. We have considered the Pt (111) surface as the model catalyst (details of the calculations are given in the STAR Methods).

In order to calculate the dissociation energy of water, we explicitly arranged water molecules in different patterns above the Pt (111) surface to model the three different coordination environments as shown in Figure 7. For free water structure, we put one water molecule above the Pt surface corresponding to a coverage of 1/9 (Figure 7A). In this case, there are no other water molecules in the simulation cell, and thus no hydrogen bonds, giving the free water structure. For trihedral coordination, we put one layer of hexagonal water (6 water molecules) above the Pt surface at a coverage of two-thirds. Ogaswara et al. have observed experimentally that the water structure above the Pt (111) surface forms a hexagonal ice-like pattern (Ogasawara et al., 2002). Previous DFT studies also reported that the geometry of water
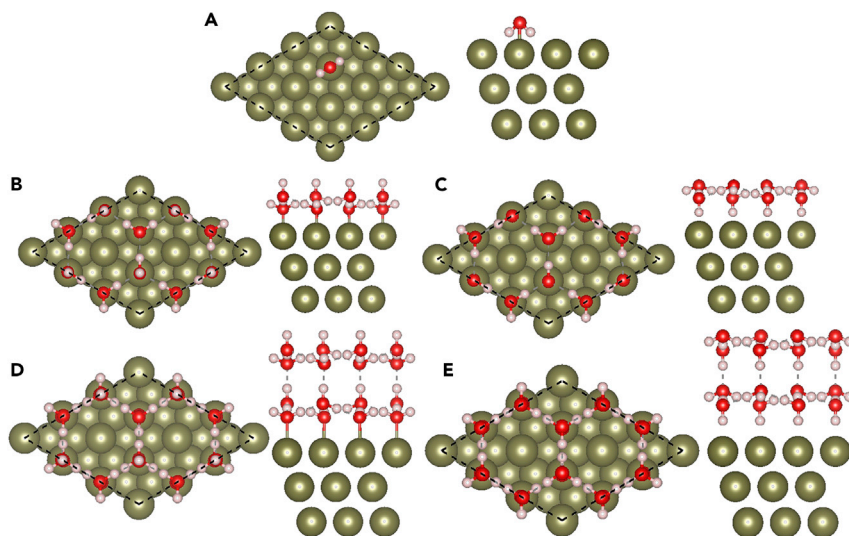
Figure 7. Free, trihedral and tetrahedral coordination of water at the electrode surface
Top and side views of (A) free, (B) trihedral-up, (C) trihedral-down, (D) tetrahedral-up, and (E) tetrahedral-down water structures above Pt (111) surface. Pt, O, and H atoms are represented by olive, red, and white spheres, respectively.

molecules above the metal surface is based on crystalline ice structure arranged in a hexagonal pattern (Chen et al., 2018; Meng et al., 2004; Michaelides, 2006; Sakong et al., 2015; Würger et al., 2020). As shown in the Figures 7B and 7C, alternate water molecules (3 out of 6) have both O−H bonds oriented parallel to the metal surface. The remaining water molecules have one O−H bond parallel to the surface. The other O−H bond can be either vertically up or down toward the surface. Accordingly, these two structures are named as trihedral-up (tri-up) and trihedral-down (tri-down) structures. In both these structures, each water molecule forms three hydrogen bonds with the neighboring ones. For tetrahedral arrangement, we have added a second hexagonal ice-like layer of water molecules above the trihedral arrangement. As a result, each water molecule now makes four hydrogen bonds, giving rise to tetrahedral coordination (Figures 7D and 7E). As in the trihedral structure, there are also two different configurations for the tetrahedral structure. These are named as tetrahedral-up (tetra-up) and tetrahedral-down (tetra-down) based on the orientation (up or down) of the O−H bonds in the water molecules in the first layer above the surface.

To search for the minimum energy paths (MEP) and corresponding barriers for the dissociation of water molecules, the climbing nudged elastic band (CI-NEB) method (Henkelman et al., 2000) has been employed. By the linear interpolation between the initial and final states, five images are created, which are optimized to map the MEP accurately.

The tri-down and tetra-down structures were found to have lower energies compared with the tri-up and tetra-up structures, respectively. This is somewhat expected based on our knowledge that Pt−H bonds are stronger than Pt−O bonds. Therefore, we considered the tri-down (Figure 7C) and tetra-down (Figure 7E) structures for dissociation barrier calculations. In both the cases, one of the molecules directed toward the metal surface dissociates. It is found that after dissociation, the intact O−H bond remains parallel to the surface, whereas the dissociated H atom gets adsorbed on a nearby Pt site. Because the metal surface provides catalytically active sites, it is only reasonable that one of the molecules directed toward the surface dissociates. The initial water structures and their corresponding transition states and the final dissociated structures are shown in the insets of Figure 8. In the free structure, the activation barrier is found to be 0.72 eV. For the trihedral structure, the value is slightly higher and is 0.88 eV. On the other hand, the activation barrier for the tetrahedral structure turns out to be 1.71 eV, much higher than the other two structures. The MEP of the Volmer reaction for three different water structures are shown in Figure 8. These results clearly indicate that a much larger kinetic barrier has to be overcome for dissociation of an O−H bond in tetrahedrally coordinated water compared with free and trihedral water. This is likely due to the more compact network of hydrogen bonds in the former. The activation energy of water dissociation indeed increases in the order free water < trihedrally coordinated water < tetrahedrally coordinated water, leading to a reverse order of their dissociation rate, and hence the rate of the Volmer step. Thus, we can
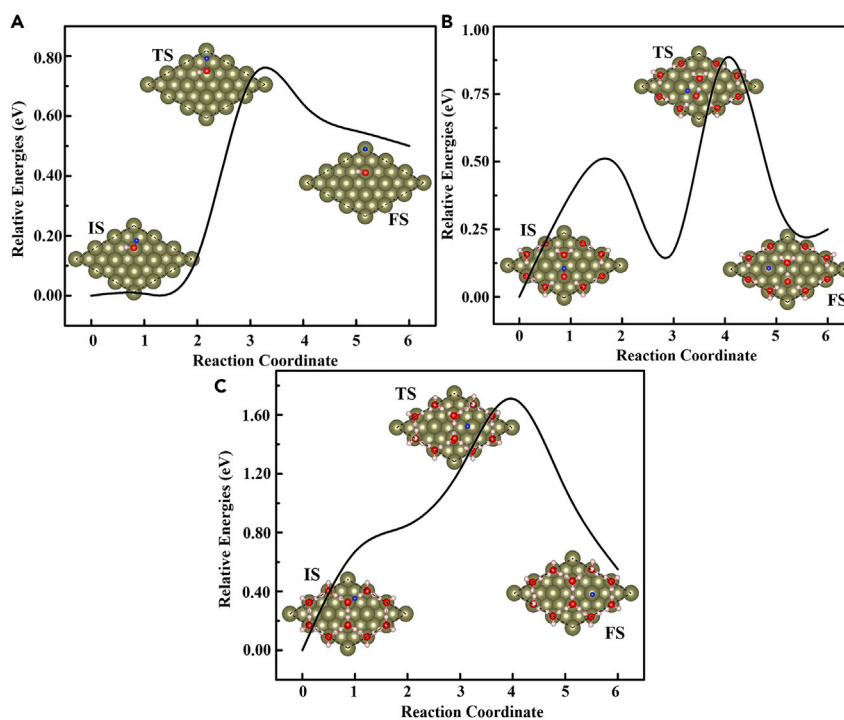
Figure 8. Minimum energy paths for dissociation of free, trihedrally and tetrahedrally coordinated water molecules

The minimum energy path (MEP) of the Volmer reaction of (A) free, (B) trihedrally coordinated, and (C) tetrahedrally coordinated water structures on Pt (111) surface calculated through NEB. The NEB computation consists of five images. Top views of initial (IS), transition (TS), and final (FS) states of different coordinated water structures are shown in the insets. Pt, O, and H atoms are represented by olive, red, and white spheres respectively. The dissociated H atom is represented by blue sphere.

convincingly ascribe the observed slowdown of the HER rate with increasing alkali concentration to the increase in population of tetrahedrally coordinated water that has the largest dissociation barrier.

Conclusion

This study unravels the changes in the water coordination with alkaline electrolyte concentration and the effect of such changes in electrochemical hydrogen generation process. Water structure becomes more tetrahedrally coordinated as the alkalinity is increased from 0.1 M to 6 M, irrespective of the counter cations ($Na^+/K^+/Rb^+$). First principles DFT calculations also show the increase in the activation energy for water dissociation (Volmer step) as the water coordination becomes more tetrahedral. We have employed *ex situ* and *in situ* Raman, ^{1}H NMR, and *ATR FTIR* spectroscopic analyses to demonstrate the reason behind the poor HER activity of *polycrystalline* Pt electrode in highly alkaline electrolytes such as KOH/NaOH/RbOH with varying concentration from 0.1 M to 6 M. According to the DFT-based calculations, the order of activation energy for water dissociation in different water structures varies as tetrahedrally coordinated water > trihedrally coordinated water > free water. This is in support of the electrocatalytic HER analyses conducted using LSVs, EIS, Tafel slope analyses, and CV based studies, where the HER activity is found to decrease in high alkaline conditions. Apart from the studies on the changes in bulk water structure, *in situ* SHINERS gave evidence toward the changes in the water structure of interfacial (electrode-electrolyte) water, where with increasing the applied potential (cathodic), the tetrahedrally coordinated water present in the interface gradually converted to trihedrally coordinated water. On the other hand, the −OH stretching mode has almost no effect on the anodic potentials (toward OER), where no changes in the water structure with potential was observed. Hence, this study establishes a new descriptor for HER in alkaline condition—water coordination, where it may help to understand many such charge transfer phenomena happening in high alkaline conditions.

STAR★METHODS

Detailed methods are provided in the online version of this paper and include the following:

- KEY RESOURCES TABLE
- RESOURCE AVAILABILITY
  - Lead contact
  - Materials availability
  - Data and code availability
- EXPERIMENTAL METHOD AND SUBJECT DETAILS
  - Electrochemical measurements
  - Electrochemical surface area (ECSA) calculation
  - ^{1}H NMR
  - Synthesis of SiO_2 coated Au nanoparticle
  - *Ex situ* Raman spectroscopy
  - *In situ* Raman spectroscopy
  - *ATR- FTIR*
  - Computational methodology

SUPPLEMENTAL INFORMATION

Supplemental information can be found online at https://doi.org/10.1016/j.isci.2022.104835.

AUTHOR CONTRIBUTIONS

A.G. and T.N.N. conceptualized and designed the project. A.G. performed the experiments. A.G. and T.N.N. analyzed the experimental data. D.K.R. and A.G. performed the ^{1}H NMR and analyzed the data. M.S, K.A., and P.S. performed the DFT-based calculations and analyzed the data. A.G., P.S and T.N.N. discussed with all the authors to writing the paper. All authors have agreed to this version of the manuscript.

DECLARATION OF INTERESTS

Authors declare no conflict of interest.

REFERENCES

Ataka, K.I., and Osawa, M. (1998). In situ infrared study of water-sulfate coadsorption on gold(111) in sulfuric acid solutions. Langmuir *14*, 951–959. https://doi.org/10.1021/la971110v.

Barbara, R., and Aroulmoji, V. (2020). FT-IR study of the hydration of caffeine, sucrose, and their mixtures in water. In Water Properties of Food, Pharmaceutical, and Biological Materials (CRC Press), pp. 623–632. https://doi.org/10.1201/9781420001181-51.

Bewick, A., and Russell, J.W. (1982). Structural investigation by infra-red spectroscopy of adsorbed hydrogen on platinum. J. Electroanal.

Chem. Interfacial Electrochem. *132*, 329–344. https://doi.org/10.1016/0022-0728(82)85029-8.

Botti, A., Bruni, F., Imberti, S., Ricci, M.A., and Soper, A.K. (2004). Ions in water: the microscopic structure of concentrated NaOH solutions. J. Chem. Phys. *120*, 10154–10162. https://doi.org/10.1063/1.1705572.

Chen, X., McCrum, I.T., Schwarz, K.A., Janik, M.J., and Koper, M.T.M. (2017). Co-Adsorption of cations as the cause of the apparent pH dependence of hydrogen adsorption on a stepped platinum single-crystal electrode.

Angew. Chem. Int. Ed. Engl. *56*, 15025–15029. https://doi.org/10.1002/anie.201709455.

Chen, L.D., Bajdich, M., Martirez, J.M.P., Krauter, C.M., Gauthier, J.A., Carter, E.A., Luntz, A.C., Chan, K., and Nørskov, J.K. (2018). Understanding the apparent fractional charge of protons in the aqueous electrochemical double layer. Nat. Commun. *9*, 3202. https://doi.org/10.1038/s41467-018-05511-y.

Cheng, T., Wang, L., Merinov, B.V., and Goddard, W.A. (2018). Explanation of dramatic pH-dependence of hydrogen binding on noble metal electrode: greatly weakened water adsorption at

high pH. J. Am. Chem. Soc. *140*, 7787–7790. https://doi.org/10.1021/jacs.8b04006.

Danilovic, N., Subbaraman, R., Strmcnik, D., Chang, K.C., Paulikas, A.P., Stamenkovic, V.R., and Markovic, N.M. (2012). Enhancing the alkaline hydrogen evolution reaction activity through the bifunctionality of Ni(OH)2/metal catalysts. Angew. Chem. Int. Ed. Engl. *51*, 12495–12498. https://doi.org/10.1002/anie.201204842.

Dubouis, N., Lemaire, P., Mirvaux, B., Salager, E., Deschamps, M., and Grimaud, A. (2018). The role of the hydrogen evolution reaction in the solid-electrolyte interphase formation mechanism for ": Water-in-Salt " electrolytes. Energy Environ. Sci. *11*, 3491–3499. https://doi.org/10.1039/c8ee02456a.

Faid, A.Y., Barnett, A.O., Seland, F., and Sunde, S. (2020). Ni/NiO nanosheets for alkaline hydrogen evolution reaction: in situ electrochemical-Raman study. Electrochim. Acta *361*, 137040. https://doi.org/10.1016/j.electacta.2020.137040.

Gilliam, R., Graydon, J., Kirk, D., and Thorpe, S. (2007). A review of specific conductivities of potassium hydroxide solutions for various concentrations and temperatures. Int. J. Hydrogen Energy *32*, 359–364. https://doi.org/10.1016/j.ijhydene.2006.10.062.

Gonella, G., Backus, E.H.G., Nagata, Y., Bonthuis, D.J., Loche, P., Schlaich, A., Netz, R.R., Kühnle, A., McCrum, I.T., Koper, M.T.M., et al. (2021). Water at charged interfaces. Nat. Rev. Chem. *5*, 466–485. https://doi.org/10.1038/s41570-021-00293-2.

Guha, A., and Narayanan, T.N. (2020). Effect of "water-in-salt" electrolytes in the electrochemical hydrogen evolution reaction of carbon nanotubes. J. Phys. Energy *2*, 034001. https://doi.org/10.1088/2515-7655/ab8e25.

Guha, A., Narayanaru, S., and Narayanan, T.N. (2018a). Tuning the hydrogen evolution reaction on metals by lithium salt. ACS Appl. Energy Mater. *1*, 7116–7122. https://doi.org/10.1021/acsaem.8b01546.

Guha, A., Veettil Vineesh, T., Sekar, A., Narayanaru, S., Sahoo, M., Nayak, S., Chakraborty, S., and Narayanan, T.N. (2018b). Mechanistic insight into enhanced hydrogen evolution reaction activity of ultrathin hexagonal boron nitride-modified Pt electrodes. ACS Catal. *8*, 6636–6644. https://doi.org/10.1021/acscatal.8b00938.

Guha, A., Kaley, N.M., Mondal, J., and Narayanan, T.N. (2020). Engineering the hydrogen evolution reaction of transition metals: effect of Li ions. J. Mater. Chem. A *8*, 15795–15808. https://doi.org/10.1039/c9ta12926j.

Du, H., Rasaiah, J.C., and Miller, J.D. (2007). Structural and dynamic properties of concentrated alkali halide solutions: a molecular dynamics simulation study. J. Phys. Chem. B *111*, 209–217. https://doi.org/10.1021/jp064659o.

Henkelman, G., Uberuaga, B.P., and Jónsson, H. (2000). Climbing image nudged elastic band method for finding saddle points and minimum energy paths. J. Chem. Phys. *113*, 9901–9904. https://doi.org/10.1063/1.1329672.

Huang, Y.F., Kooyman, P.J., and Koper, M.T.M. (2016). Intermediate stages of electrochemical oxidation of single-crystalline platinum revealed by in situ Raman spectroscopy. Nat. Commun. *7*, 12440. https://doi.org/10.1038/ncomms12440.

Huang, B., Rao, R.R., You, S., Hpone Myint, K., Song, Y., Wang, Y., Ding, W., Giordano, L., Zhang, Y., Wang, T., et al. (2021). Cation- and pH-dependent hydrogen evolution and oxidation reaction kinetics. JACS Au *1*, 1674–1687. https://doi.org/10.1021/jacsau.1c00281.

Kresse, G., and Hafner, J. (1994). Ab initio molecular-dynamics simulation of the liquid-metalamorphous- semiconductor transition in germanium. Phys. Rev. B Condens. Matter *49*, 14251–14269. https://doi.org/10.1103/PhysRevB.49.14251.

Kresse, G., and Furthmüller, J. (1996). Efficiency of ab-initio total energy calculations for metals and semiconductors using a plane-wave basis set. Comput. Mater. Sci. *6*, 15–50. https://doi.org/10.1016/0927-0256(96)00008-0.

Kresse, G., and Joubert, D. (1999). From ultrasoft pseudopotentials to the projector augmented-wave method. Phys. Rev. B *59*, 1758–1775. https://doi.org/10.1103/PhysRevB.59.1758.

Kunimatsu, K., Senzaki, T., Tsushima, M., and Osawa, M. (2005). A combined surface-enhanced infrared and electrochemical kinetics study of hydrogen adsorption and evolution on a Pt electrode. Chem. Phys. Lett. *401*, 451–454. https://doi.org/10.1016/j.cplett.2004.11.100.

Kunimatsu, K., Uchida, H., Osawa, M., and Watanabe, M. (2006). In situ infrared spectroscopic and electrochemical study of hydrogen electro-oxidation on Pt electrode in sulfuric acid. J. Electroanal. Chem. *587*, 299–307. https://doi.org/10.1016/j.jelechem.2005.11.026.

Kunimatsu, K., Senzaki, T., Samjeské, G., Tsushima, M., and Osawa, M. (2007). Hydrogen adsorption and hydrogen evolution reaction on a polycrystalline Pt electrode studied by surface-enhanced infrared absorption spectroscopy. Electrochim. Acta *52*, 5715–5724. https://doi.org/10.1016/j.electacta.2006.12.007.

Laursen, A.B., Varela, A.S., Dionigi, F., Fanchiu, H., Miller, C., Trinhammer, O.L., Rossmeisl, J., and Dahl, S. (2012). Electrochemical hydrogen evolution: sabatier ' s principle and the volcano plot. J. Chem. Educ. *89*, 1595–1599. https://doi.org/10.1021/ed200818t.

Ledezma-Yanez, I., Wallace, W.D.Z., Sebastián-Pascual, P., Climent, V., Feliu, J.M., and Koper, M.T.M. (2017). Interfacial water reorganization as a pH-dependent descriptor of the hydrogen evolution rate on platinum electrodes. Nat. Energy *2*, 17031. https://doi.org/10.1038/nenergy.2017.31.

Li, J.F., Huang, Y.F., Duan, S., Pang, R., Wu, D.Y., Ren, B., Xu, X., and Tian, Z.Q. (2010). SERS and DFT study of water on metal cathodes of silver, gold and platinum nanoparticles. Phys. Chem. Chem. Phys. *12*, 2493–2502. https://doi.org/10.1039/b919266b.

Li, J.F., Tian, X.D., Li, S.B., Anema, J.R., Yang, Z.L., Ding, Y., Wu, Y.F., Zeng, Y.M., Chen, Q.Z., Ren, B., et al. (2013). Surface analysis using shell-isolated nanoparticle-enhanced Raman spectroscopy.

Nat. Protoc. *8*, 52–65. https://doi.org/10.1038/nprot.2012.141.

Li, C.Y., Le, J.B., Wang, Y.H., Chen, S., Yang, Z.L., Li, J.F., Cheng, J., and Tian, Z.Q. (2019). In situ probing electrified interfacial water structures at atomically flat surfaces. Nat. Mater. *18*, 697–701. https://doi.org/10.1038/s41563-019-0356-x.

Liu, E., Li, J., Jiao, L., Doan, H.T.T., Liu, Z., Zhao, Z., Huang, Y., Abraham, K.M., Mukerjee, S., Jia, Q., and Jia, Q. (2019). Unifying the hydrogen evolution and oxidation reactions kinetics in base by identifying the catalytic roles of hydroxyl-water-cation adducts. J. Am. Chem. Soc. *141*, 3232–3239. https://doi.org/10.1021/jacs.8b13228.

Mahmood, N., Yao, Y., Zhang, J.W., Pan, L., Zhang, X., and Zou, J.J. (2018). Electrocatalysts for hydrogen evolution in alkaline electrolytes: mechanisms, challenges, and prospective solutions. Adv. Sci. *5*, 1700464. https://doi.org/10.1002/advs.201700464.

McCrum, I.T., and Janik, M.J. (2016). pH and alkali cation effects on the Pt cyclic voltammogram explained using density functional theory. J. Phys. Chem. C *120*, 457–471. https://doi.org/10.1021/acs.jpcc.5b10979.

Meng, S., Wang, E.G., and Gao, S. (2004). Water adsorption on metal surfaces: a general picture from density functional theory studies. Phys. Rev. B - Condens. Matter *69*, 195404. https://doi.org/10.1103/PhysRevB.69.195404.

Michaelides, A. (2006). Density functional theory simulations of water-metal interfaces: waltzing waters, a novel 2D ice phase, and more. Appl. Phys. A *85*, 415–425. https://doi.org/10.1007/s00339-006-3695-9.

Morales-Guio, C.G., Stern, L.A., and Hu, X. (2014). Nanostructured hydrotreating catalysts for electrochemical hydrogen evolution. Chem. Soc. Rev. *43*, 6555–6569. https://doi.org/10.1039/c3cs60468c.

Nørskov, J.K., Bligaard, T., Logadottir, A., Kitchin, J.R., Chen, J.G., Pandelov, S., and Stimming, U. (2005). Trends in the exchange current for hydrogen evolution. J. Electrochem. Soc. *152*, J23–J26. https://doi.org/10.1149/1.1856988.

Ogasawara, H., and Ito, M. (1994). Hydrogen adsorption on Pt(100), Pt(110), Pt(111) and Pt(1111) electrode surfaces studied by in situ infrared reflection absorption spectroscopy. Chem. Phys. Lett. *221*, 213–218. https://doi.org/10.1016/0009-2614(94)00247-9.

Ogasawara, H., Brena, B., Nordlund, D., Nyberg, M., Pelmenschikov, A., Pettersson, L.G.M., and Nilsson, A. (2002). Structure and bonding of water on Pt(111). Phys. Rev. Lett. *89*, 276102. https://doi.org/10.1103/PhysRevLett.89.276102.

Ojha, K., Doblhoff-Dier, K., and Koper, M.T.M. (2022). Double-layer structure of the Pt(111)-aqueous electrolyte interface. Proc. Natl. Acad. Sci. USA *119*, e2116016119. https://doi.org/10.1073/pnas.2116016119.

Oka, K., Shibue, T., Sugimura, N., Watabe, Y., Winther-Jensen, B., and Nishide, H. (2019). Long-lived water clusters in hydrophobic solvents investigated by standard NMR techniques. Sci.

Rep. 9, 223–224. https://doi.org/10.1038/s41598-018-36787-1.

Perdew, J.P., Burke, K., and Ernzerhof, M. (1996). Generalized gradient approximation made simple. Phys. Rev. Lett. 77, 3865–3868. https://doi.org/10.1103/PhysRevLett.77.3865.

Ramaker, D.E., and Roth, C. (2015). Nature of the intermediate binding sites in hydrogen oxidation/evolution over Pt in alkaline and acidic media. ChemElectroChem 2, 1582–1594. https://doi.org/10.1002/celc.201500111.

Ren, B., Xu, X., Li, X.Q., Cai, W.B., and Tian, Z.Q. (1999). Extending surface Raman spectroscopic studies to transition metals for practical applications. II. hydrogen adsorption at platinum electrodes. Surf. Sci. 427–428, 157–161. https://doi.org/10.1016/S0039-6028(99)00257-5.

Sakong, S., Naderian, M., Mathew, K., Hennig, R.G., and Groß, A. (2015). Density functional theory study of the electrochemical interface between a Pt electrode and an aqueous electrolyte using an implicit solvent method. J. Chem. Phys. 142, 234107. https://doi.org/10.1063/1.4922615.

Sarabia, F.J., Sebastián-Pascual, P., Koper, M.T.M., Climent, V., and Feliu, J.M. (2019). Effect of the interfacial water structure on the hydrogen evolution reaction on Pt(111) modified with different nickel hydroxide coverages in alkaline media. ACS Appl. Mater. Interfaces 11, 613–623. https://doi.org/10.1021/acsami.8b15003.

Seki, T., Chiang, K.Y., Yu, C.C., Yu, X., Okuno, M., Hunger, J., Nagata, Y., and Bonn, M. (2020). The bending mode of water: a powerful probe for hydrogen bond structure of aqueous systems. J. Phys. Chem. Lett. 11, 8459–8469. https://doi.org/10.1021/acs.jpclett.0c01259.

Shen, L., Lu, B., Li, Y., Liu, J., Huang-fu, Z., Peng, H., Ye, J., Qu, X., Zhang, J., Li, G., et al. (2020). Interfacial structure of water as a new descriptor of the hydrogen evolution reaction. Angew. Chem. Int. Ed. Engl. 132, 22583–22588. https://doi.org/10.1002/ange.202007567.

Sheng, W., Zhuang, Z., Gao, M., Zheng, J., Chen, J.G., and Yan, Y. (2015). Correlating hydrogen oxidation and evolution activity on platinum at different pH with measured hydrogen binding energy. Nat. Commun. 6, 5848. https://doi.org/10.1038/ncomms6848.

Shinagawa, T., Garcia-esparza, A.T., and Takanabe, K. (2015). Insight on Tafel slopes from a microkinetic analysis of aqueous electrocatalysis for energy conversion. Sci. Rep. 5, 13801. https://doi.org/10.1038/srep13801.

Stefanski, J., Schmidt, C., and Jahn, S. (2018). Aqueous sodium hydroxide (NaOH) solutions at high pressure and temperature: insights from: in situ Raman spectroscopy and ab initio molecular dynamics simulations. Phys. Chem. Chem. Phys. 20, 21629–21639. https://doi.org/10.1039/c8cp00376a.

Subbaraman, R., Tripkovic, D., Strmcnik, D., Chang, K.C., Uchimura, M., Paulikas, a.P., Stamenkovic, V., and Markovic, N.M. (2011). Enhancing hydrogen evolution activity in water splitting by tailoring Li$^+$-Ni(OH)$_2$-Pt interfaces. Science 334, 1256–1260.

Wang, X., Xu, C., Jaroniec, M., Zheng, Y., and Qiao, S.Z. (2019). Anomalous hydrogen evolution behavior in high-pH environment induced by locally generated hydronium ions. Nat. Commun. 10, 4876. https://doi.org/10.1038/s41467-019-12773-7.

Wang, Y., Li, F., Wang, C., Fang, W., Sun, C., and Men, Z. (2020). Enhanced stimulated Raman

scattering of water by KOH. Opt. Express 28, 9533–9540. https://doi.org/10.1364/oe.389681.

Würger, T., Feiler, C., Vonbun-Feldbauer, G.B., Zheludkevich, M.L., and Meißner, R.H. (2020). A first-principles analysis of the charge transfer in magnesium corrosion. Sci. Rep. 10, 15006–15011. https://doi.org/10.1038/s41598-020-71694-4.

Xue, S., Garlyyev, B., Watzele, S., Liang, Y., Fichtner, J., Pohl, M.D., and Bandarenka, A.S. (2018). Influence of alkali metal cations on the hydrogen evolution reaction activity of Pt, Ir, Au, and Ag electrodes in alkaline electrolytes. ChemElectroChem 5, 2326–2329. https://doi.org/10.1002/celc.201800690.

Yu, X., Zhao, J., Zheng, L.-R., Tong, Y., Zhang, M., Xu, G., Li, C., Ma, J., and Shi, G. (2018). Hydrogen evolution reaction in alkaline media: alpha- or beta-nickel hydroxide on the surface of platinum? ACS Energy Lett. 3, 237–244. https://doi.org/10.1021/acsenergylett.7b01103.

Zheng, J., Nash, J., Xu, B., and Yan, Y. (2018). Perspective—towards establishing apparent hydrogen binding energy as the descriptor for hydrogen oxidation/evolution reactions. J. Electrochem. Soc. 165, H27–H29. https://doi.org/10.1149/2.0881802jes.

Zhu, S., Qin, X., Yao, Y., and Shao, M. (2020). PH-dependent hydrogen and water binding energies on platinum surfaces as directly probed through surface-enhanced infrared absorption spectroscopy. J. Am. Chem. Soc. 142, 8748–8754. https://doi.org/10.1021/jacs.0c01104.

Zhu, S., and Shao, M. (2022). Electrolyte pH-dependent hydrogen binding energies and coverages on platinum, iridium, rhodium, and ruthenium surfaces. Catal. Sci. Technol. 12, 3228–3233. https://doi.org/10.1039/d2cy00385f.

STAR★METHODS

KEY RESOURCES TABLE

REAGENT or RESOURCE	SOURCE	IDENTIFIER
Chemicals		
NaOH	Sigma Aldrich	CAS # 1310-73-2
KOH	Sigma Aldrich	CAS # 1310-58-3
RbOH	Sigma Aldrich	CAS # 12026-05-0
Pt/C (20 wt%)	Sigma Aldrich	Product # 738549
Nafion (5 wt%)	Sigma Aldrich	CAS # 31175-20-9
Sodium trimethylsilylpropanesulfonate (DSS, NMR standard)	Sigma Aldrich	CAS # 2039-96-5
D_2O	Sigma Aldrich	CAS # 7789-20-0
Sodium Citrate	Sigma Aldrich	CAS # 6132-04-3
$HAuCl_4$	Sigma Aldrich	CAS # 16961-25-4
(3-aminopropyl)triethoxysilane (APTES)	Sigma Aldrich	CAS # 919-30-2
Sodium silicate	Sigma Aldrich	Product # 338443-1L
Software and algorithms		
OriginPro	OriginLab	V2021
Vienna Ab initio Simulation Package (VASP)	–	VASP 5.4.4

RESOURCE AVAILABILITY

Lead contact

Information and requests for resources should be directed to and will be fulfilled by the lead author, T N Narayanan (tnn@tifrh.res.in (T.N.N.)).

Materials availability

This study does not generate any unique reagent.

Data and code availability

- Data reported in this paper will be shared by the lead contact upon request.

- This paper does not report original codes.

- Any additional information required to reanalyze the data reported in this paper is available from the lead contact upon request.

EXPERIMENTAL METHOD AND SUBJECT DETAILS

Electrochemical measurements

All the electrochemical measurements were performed by a single channel Biologic SP-200 potentiostat in argon (Ar) saturated electrolyte. A three-electrodes set up was used for all the experiments. Ag/AgCl (saturated KCl, potential 0.197 V vs. RHE) was used as reference electrode and graphite rod was used as counter electrode. All the potentials were converted to RHE scale by using the following formula $E_{RHE} = E_{Ag/AgCl} + 0.197 + 0.0591* pH$. Before performing any electrolysis, the glassy carbon electrode or Pt electrode (3mm diameter) was polished with alumina powder (particle size $\sim$3 μm). For the sample ink preparation, 5 mg of Pt/C (20 wt%), was mixed in 1 mL of water-ethanol (3:1) and 50 μL of 5 wt% Nafion solution was used as binder. 2 μL of the as prepared ink was drop casted on glassy carbon electrode (3 mm diameter, 0.07 cm² geometrical area) and dried under room temperature. The loading of the sample was kept as 0.136 mg/cm². Before taking the linear sweep voltammograms (LSVs), Pt or Pt/C modified glassy carbon electrode was cycled for 10 times from 0.1 V vs. RHE to 1.6V vs. RHE at 200 mV/s scan rate and also cycled

in the HER region for 10 times for activation at scan rate of 50 mV/s from 0.96 V vs. RHE (for 0.1 M) and 1.02 V vs. RHE (for 1, 3 and 6 M) to −0.18 V vs. RHE (for both 0.1, 1, 3, and 6 M). The LSVs were taken at a scan rate of 50 mV/s. The CVs of all the electrocatalysts were taken at 200 mV/s.

All the electrochemical impedance spectra (EIS) were taken at −0.075 V vs. RHE from 7 MHz to 100 mHz with a varying sine wave potential having an amplitude of 10 mV. The Nyquist plots were best fitted by the simulated Randles circuits (R(RC)).

Electrochemical surface area (ECSA) calculation

Electrochemical surface area of Pt/C was calculated from the anodic under potential deposition region of hydrogen (desorption of H_{UPD}) (Table S2) using the charge density value for Pt as 210 $\mu C/cm^2$ (Guha et al., 2018a, 2018b). For the ECSA calculation a linear sweep voltammetry was used with a step size of 50 mV/s or 200 mV/s.

^1H NMR

^1H NMR spectra were measured by a 300 MHz Bruker Nano Bay spectrometer. All the NMR data were recorded at 25°C with a spectral width of 12 ppm (8 scans) having water pre-saturation using a coaxial tube. 10% D_2O water was inserted in the inner tube and as prepared electrolyte with varying the concentration of KOH/NaOH/RbOH was inserted in the outer tube. For the standard ^1H NMR experiment, 10 mM DSS in 10% D_2O in water was used in the inner tube.

Synthesis of SiO_2 coated Au nanoparticle

SiO_2 coated Au nanoparticle (55 nm) were synthesized using a method reported elsewhere (Li et al., 2013, 2019). Initially, 200 mL 0.01 wt% $HAuCl_4$ was boiled at 140°C and then 1.4 mL 1 wt% sodium citrate was added to synthesize Au np (55nm) which was stored in refrigerator. 30 mL as prepared sample was mixed with 0.4 mL 1 mM (3-aminopropyl)triethoxysilane (APTES) and then 0.54 wt% 3.2 mL of sodium silicate with a pH of ~10 was added to the solution. Then the mixture was transferred to 95°C bath and stirred for 30 min. As prepared SiO_2 coated Au np was centrifuged twice and washed with DI water and concentrated solution was kept in refrigerator. The concentrated solution was diluted and dropcasted on *polycrystalline* Pt electrode before the *in situ* electrochemical SHINERS experiment.

Ex situ Raman spectroscopy

Raman spectra were taken using a micro-Raman spectrometer (Renishaw Invia Spectrometer) with 532 nm laser excitation using L50x lens. The time for recording data was optimized to 10 s for a better signal-to-noise ratio.

In situ Raman spectroscopy

In situ SHINERS were taken using a micro-Raman spectrometer (Renishaw Invia Spectrometer) with 633 nm laser excitation using L50x lens using a homemade electrochemical cell as shown in Figure S12. The time for recording data was optimized to 10 s for a better signal-to-noise ratio.

All the Raman spectra are taken in reflection mode using an edge filter where only Stokes lines can be observed.

ATR- FTIR

All the Fourier transform infrared spectroscopy – attenuated total reflectance (*ATR-FTIR*) measurements were performed by a Thermo Fischer scientific Nicolet iS50 FTIR spectrometer in attenuated total reflectance mode from 500 cm^{-1} to 4000 cm^{-1}.

Computational methodology

All energies of different Pt(111)/water interface structures were calculated using plane wave DFT as implemented in the Vienna *Ab initio* Simulation Package (VASP) (Kresse and Furthmüller, 1996; Kresse and Hafner, 1994; Kresse and Joubert, 1999). The projector augmented wave (PAW) potential was used to describe the interactions between ion cores and valence electrons. An energy cut-off of 500 eV was used to describe the plane-wave basis set. The exchange-correlation energy was calculated using the Perdew-Burke-Ernzerhof (PBE) version of generalized gradient approximation (GGA) (Perdew et al., 1996). The convergence criteria for

electronic self-consistency and geometry optimization were set at 10^{-5}eV and 0.05 eV/Å respectively. The Pt(111) surface was modeled by a slab that is 3x3 in-plane with three atomic layers. Each layer contains 9 Pt atoms. A vacuum of 25 Å was maintained perpendicular to the slab to avoid the interactions between images created due to periodicity. A 5x5x1 k-point grid was used to sample the Brillouin zone.